# Visualization of freestream vortices in the NASA Langley 4-Foot Supersonic Unitary Plan Wind Tunnel

Ross A Burns[1,*], Timothy W Fahringer, Jr.[2], Paul M Danehy[2]

1: ViGYAN, Inc., USA
2: NASA Langley Research Center, USA
* Correspondent author: ross.a.burns@nasa.gov

**Keywords**: Flow visualization, vortex, supersonic, pulse-burst

## ABSTRACT

Streamwise vortices present in the freestream of the NASA Langley 4-Foot Supersonic Unitary Plan Wind Tunnel have been observed experimentally for the first time. A high-energy, burst-mode laser system was used to conduct time-resolved planar laser Mie scattering in the freestream of this facility. The freestream of the facility was observed over Mach numbers ranging from 2.4 to 4.6 and (unit) Reynolds number between $3.3 \times 10^6$ to $14.8 \times 10^6$ 1/m. Apparent vortical structures were observed in the tunnel freestream at Mach numbers ≤ 3 with little difference observed for varying Reynolds number. With further-increasing Mach number, protrusive and oscillatory vertical 'sprite' structures were observed emanating from the tunnel floor boundary layer. Neither of these structural phenomena have been observed before experimentally in the facility and act to confirm and inform predictions made in computational fluid dynamic simulations of the facility.

## 1. Introduction

Ongoing efforts at the NASA Langley Research Center are motivated by the CFD vision 2030 (Slotnick 2014)(Cary 2021) and supported by the NASA Aerosciences Evaluation and Test Capabilities (AETC) portfolio (Ross 2021-1). One area of focus that is of principal concern center- and agency-wide is the role computational fluid dynamics (CFD) capabilities play in present and future research, development, and evaluation activities. For example, the continual improvements to CFD robustness have raised questions on whether experimental capabilities could be replaced by simulations, both for practical and financial reasons. Presently, the experimental capabilities remain essential for most areas of aerothermodynamic study (Childs 2021). One facility that has recently been assessed is the Langley 4-Foot Supersonic Unitary Plan Wind Tunnel (UPWT)(Jackson 1981). In these evaluations, umbrella comparisons between experimental results and *a priori* / *a posteriori* CFD were made with respect to both the empty test section and model operations (Ross 2021-1)(Ross 2021-2)(Denison 2021).

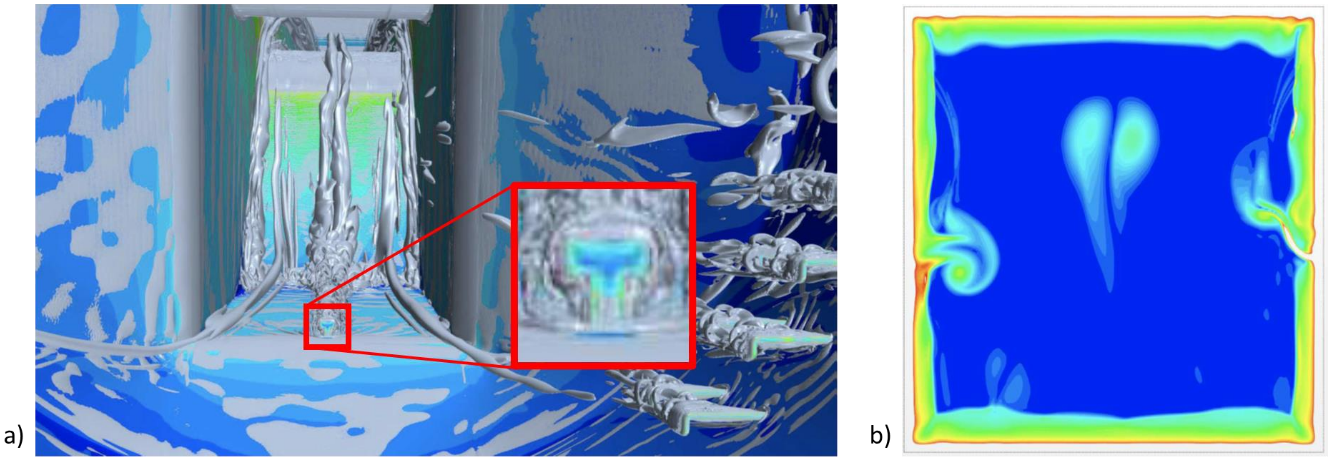

**Fig. 1** Predicted streamwise vortices in the NASA Langley UPWT. a) Isosurfaces of vorticity within the plenum showing the T-shaped rail (inset) as the origin and b) vorticity contours within the test section of the facility. Test section is 1.32 m (H) by 1.22 m (W) in b). Adapted from Childs (2021).

One point of contention for the maintenance of this experimental facility was a notable disparity in the results within the empty test section/freestream of the facility. Specifically, some simulations predicted the presence of a notable pair of streamwise vortices in the center of the test section seeming to emanate from a T-shaped rail in the plenum of the facility. Figure 1 depicts these vortices from their starting point within the plenum (Fig. 1a) and their presentation within the test section (Fig. 1b) as shown by certain simulations (Childs 2021). These vortices had not been observed experimentally, neither with measurements using hotwire probe arrays (Ross 2021)(Chou 2021) nor flow visualizations within the test section utilizing time-averaged planar laser Mie scattering (PLMS) (Danehy 2019). With the potential this vortex pair had to contaminate measurements within the facility, gaining insight into the observed disparity was essential both for understanding the simulation results and for maintaining the facility.

The present work operated in parallel with many of the previously described testing efforts. During a testing campaign in which a variation on the Doppler global velocimetry (DGV) technique was being tested in the UPWT, it was noted in some of the raw data that certain regions of the flow appeared occluded unexpectedly (circular regions absent of scattering) (Burns 2021). After learning about the predicted freestream vortices, a dedicated effort was made to determine if this effect was related to the streamwise vortices. The experiments in Ref. **Error! Bookmark not defined.** differed from the previous flow visualization efforts in the UPWT in that they utilized a high-energy, burst-mode laser with a short pulse duration (20 ns), providing a nearly frozen view of the flow during the imaging period in contrast to the time-averaged measurements that used a continuous wave (cw) laser (Morris 1985)(Birch 2000). Past measurements in UPWT utilizing this 'vapor screen' method were able to detect vortices that were positionally stable, but no such artifacts were detected in relation to the freestream vortices. This paper documents the experiments that were undertaken to visualize and (if possible) characterize the freestream vortices within the test section utilizing high-speed PLMS. Note that a very small sub-sample of these data were presented in (Childs 2021) in corroboration of their results, but this paper is much more comprehensive in detail and presentation. The paper is structured as follows: following this introduction, the experimental program will be described along with the results, discussion, and concluding remarks.

## 2. Experimental Program

This section details all aspects of the experiment setup including the facility, the laser system, and the imaging systems used in the acquisition of data.

### A. Experimental Facility

The tests were conducted in the NASA Langley 4-Foot Supersonic Unitary Plan Wind Tunnel, a large-scale supersonic test facility capable of continuous operation. The Mach number of the facility is variable from 1.47 to 4.64, achieved by utilizing a sliding nozzle block configuration. Two different test sections account for the full range of Mach numbers: Test Section 1 covers Mach numbers in the range of 1.47 to 2.87, while Test Section 2 accommodates Mach numbers ranging from 2.29 to 4.64. These tests were conducted in Test Section 2; a diagram of the nozzle block and test section of this facility is shown in Fig. 2. Test section 2 has cross-sectional dimensions of 1.32 m (H) by 1.22 m (W) and an overall length of 2.14 m. Of special note for these experiments was the presence of a T-shaped guide rail underneath the sliding nozzle block (noted in Fig. 2). This rail is partly exposed at certain Mach numbers and is thought to be the source of the streamwise vortices observed in simulations.

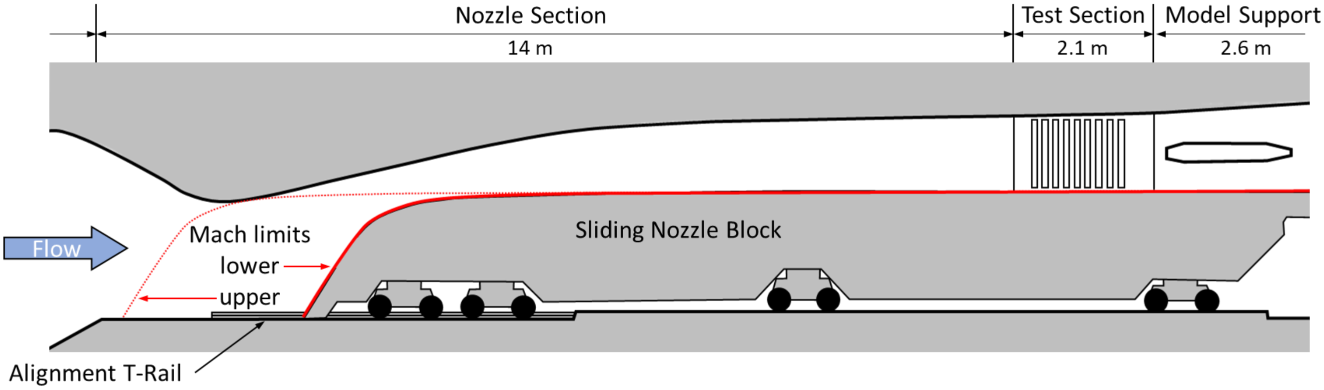

**Fig. 2** Diagram of UPWT TS2 showing sliding nozzle block and location of T-rail.

Test conditions varied for each case. The conditions were specified in terms of operating Mach number and unit Reynolds number, which ranged in these tests from 2.4 and 4.6 for the Mach number, and $3.3 \times 10^6$ 1/m to $14.8 \times 10^6$ 1/m. A summary of the combinations of the conditions tested throughout the two campaigns can be found in Table 1. The flow was seeded for flow visualization by injecting liquid water downstream of the test section. As the water circulated and homogenized throughout the facility, a fog of ice crystals developed in the nozzle and passed into the test section, which was used as the scattering medium. Note that this fog has been used in previous DGV and flow visualization experiments (Meyers 1995)(Birch 2000)(Burns 2021), and the particles that comprise the fog are generally too small for performing particle image velocimetry or similar techniques. The tunnel dew point was kept between 276.6 K (38 °F) and 291.5 K (65 °F) to maintain the desired level of seeding, with higher dew points being used at higher Mach number operation. It was observed in post-test analysis that the force and moment measurements on the model were modified slightly (a few percent) by the presence of the water vapor. During testing, a higher seed concentration was chosen to minimize the laser-pulse energy used and thus reduce the risk of damaging the facility windows. In future experiments, the balance between these parameters could be redressed to limit the effects of the measurement on the flowfield without significantly compromising the safety of the facility windows.

Optical access to the test section was afforded by a series of vertical windows arranged along each sidewall. Each window was approximately 130 mm wide and separated from the next by a 30 mm steel spar, each of which was approximately 230 mm deep. These windows (blue) and spars (black) can be seen in the overall diagram in Fig. 2 and the test section diagrams in Fig. 3 (in addition to the test section optics and camera configurations). Note also in Fig. 3 the orientation of the coordinate system. The x-direction is the streamwise direction with its origin at the beginning of the test section, the y-direction is the spanwise direction (positive pointing away from the laser system with the origin at the spanwise center of the test section), and the z-direction is the tunnel vertical direction ($+z$ pointing upward, the origin at the vertical center of the test section).

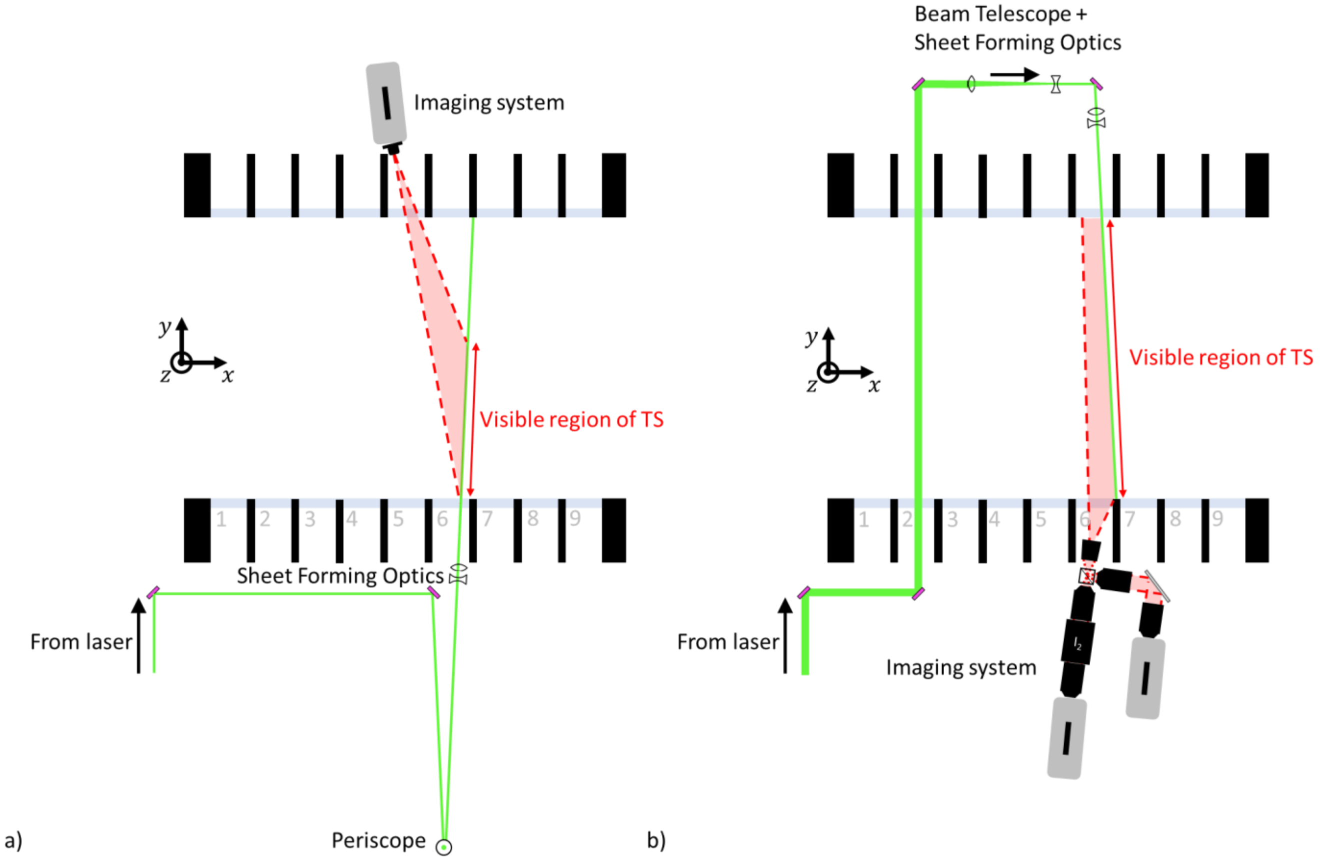

**Fig. 3** Diagram of optical and imaging systems around test section. a) first testing campaign and b) second testing campaign.

## B. Laser and Optical Systems

This section describes the laser system and optical components utilized in these experiments. Two different tests were included in these studies utilizing very similar equipment. Any specific differences will be made evident.

### *1. Laser system*

The laser used in these studies was a burst-mode, master oscillator, pulsed amplifier system (Spectral Energies QuasiModo$^{\text{TM}}$ 1200). The laser utilized an external cavity diode laser (ECDL, Sacher LiON series) as a seed laser, which allowed the laser frequency to be rapidly scanned through variation of the laser diode current or through piezo actuation. The operating frequency of the laser was set to 100 kHz, while the burst duration and period were 10 ms and 12 s, respectively. The second harmonic of this Nd:YAG system was used with the center wavelength set to 532.217 nm. A pulse duration of 20 ns was used; this duration was a compromise selected to balance capturing near-instantaneous images and reducing the risk of damaging the (very expensive) facility windows. Figure 4 presents a diagram of the primary laser system. The output from the main amplifier head is divided into two pathways: a diagnostic leg and the main experimental leg. The diagnostic leg, which was sampled by taking the small fraction of light that passed through a high-reflectivity mirror, housed the diagnostic systems used to characterize the laser output. The main experimental leg first passed through a variable attenuator ($\lambda/2$-plate and plate polarizer) and then a 1:1 (Test 1) or 1:3 (Test 2) inverting telescope with a small (500 $\mu$m) iris at its focus, which was used to help limit beam steering associated with thermal lensing during the burst (and to expand the beam diameter when the 1:3 telescope was utilized). This portion of the laser system then transmitted the beam over to the wind tunnel test section. The laser was always operated at full power, and the energy content of the beam was controlled exclusively with the variable attenuator. While a similar effect could be achieved by adjusting amplifier voltages within

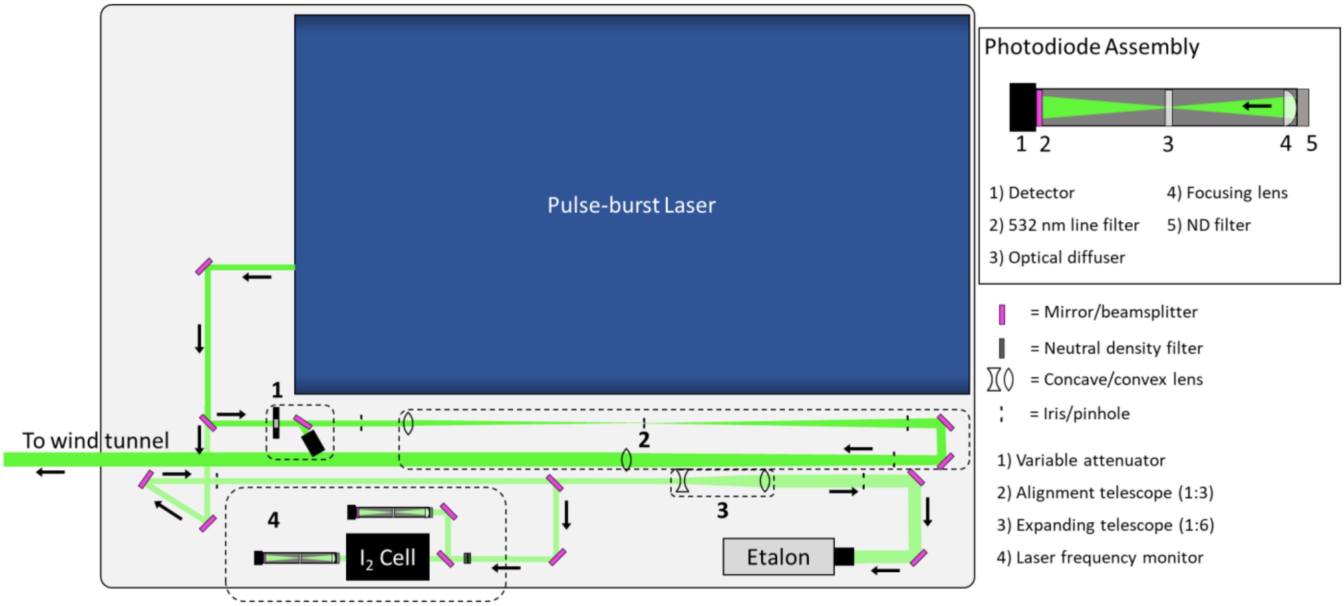

**Fig. 4** Diagram of primary laser setup.

the laser, doing so would have made both the spatial profile of the beam and the temporal profile of each burst more variable and unpredictable.

### *2. Test-section optics*

Top-view diagrams of the test section optics from both testing campaigns are found in Fig. 3. Test 1 (Fig. 3a) utilized a large laser sheet generated on the near (laser) side of the test section. After the beam was transmitted over to the area of the test section, the beam went through a 3-lens system to form the sheet: a 2-m plano-convex lens and 2 cylindrical lenses (+25.4 mm and -38 mm) spaced at 127 mm. These lenses generated a large vertical laser sheet approximately 0.48 m tall on the near window and over 1.22 m on the far window. The sheet was directed into the spar between windows 6 and 7 to act as a beam stop.

The second set of experiments (Test 2) attempted to achieve an even larger field of view (FOV). To accommodate a larger and more complex camera system, the laser sheet had to be brought into the facility from the opposite side. To achieve this, the beam was first routed through the facility far upstream of the measurement location as indicated in the figure. Receiving optics on the far side of the test section included a beam telescope, which acted as the focusing lens in this case (reducing the diameter primarily, but leaving the beam slightly converging after such that it focused at the center of the test section), and the same cylindrical lens pair used in the first experiments (+25.4 mm and -38 mm, 127 mm spacing) to expand the sheet vertically. The sheet was very similar in size but was positioned closer to the floor of the wind tunnel compared to Test 1.

### *3. Imaging systems and data acquisition*

The Test 1 experiments (Fig. 3a) utilized a high-speed CMOS camera (Photron Fastcam SA-Z), operated at 20 kHz. The camera was angled to observe the laser sheet closer to the near wall of the test section from the 5th window. A 50-mm lens was Scheimpflug-mounted to the camera to accommodate the shallow viewing angle. The FOV for these experiments with respect to the laser sheet and test section cross-section is shown in Fig. 5a. To achieve a larger FOV in Test 2, a dual-relay imaging system was implemented (Fig. 6). This system served two purposes. First, it allowed the imaging lens to be placed both closer to the window and at the correct position with respect to the laser sheet. Second, a type of DGV was performed simultaneously during these experiments, and the dual-relay system was required to allow one channel to view through an iodine cell. Details on the dual-relay imaging system and the DGV experiments can be found in Burns (2022-1). The primary imaging lens in the dual-relay system was 35 mm, and two high-speed CMOS cameras (Photron Fastcam SA-Z) were used as the imagers. Both cameras were operated at 25 kHz during these tests. The orientation of this imaging system can be seen in Fig. 3b, while the relative positions of the laser sheet and FOV in the test section is shown Fig. 5b.

Data for these tests were acquired in ‘bursts,’ i.e., a short sequence of time-resolved images corresponding to one burst from the laser. Bursts were generally 10 ms in length and captured 200 (Test 1) to 250 (Test 2) images at their respective repetition rates (capturing one of every 5 or 4 laser pulses, respectively). Test 1 and Test 2 did not necessarily acquire data at the same tunnel operating conditions. Since Test 1 was focused on vortex visualization, more and different conditions were captured than in Test 2. When data from both tests are available, they will both be presented in the following section. Test conditions for both tests are summarized in Table 1.

**Table 1** Test conditions used during Tests 1 and 2. T1 and T2 indicate test number, and bold indicates the viability of freestream visualization.

| | | **Mach #** | | | | | | | | | | | |
|---|---|---|---|---|---|---|---|---|---|---|---|---|---|
| | | 2.4 | | 2.5 | | 2.75 | | 3 | | 3.5 | | 4.6 | |
| **Re #** | $3.3\times10^6$/m | **T1** | | **T1** | | **T1** | | **T1** | | **T1** | **T2** | | |
| | $9.9\times10^6$/m | **T1** | **T2** | **T1** | | **T1** | | | | **T1** | **T2** | **T1** | **T2** |
| | $14.8\times10^6$/m | | T2 | | | | | | | | **T2** | | |

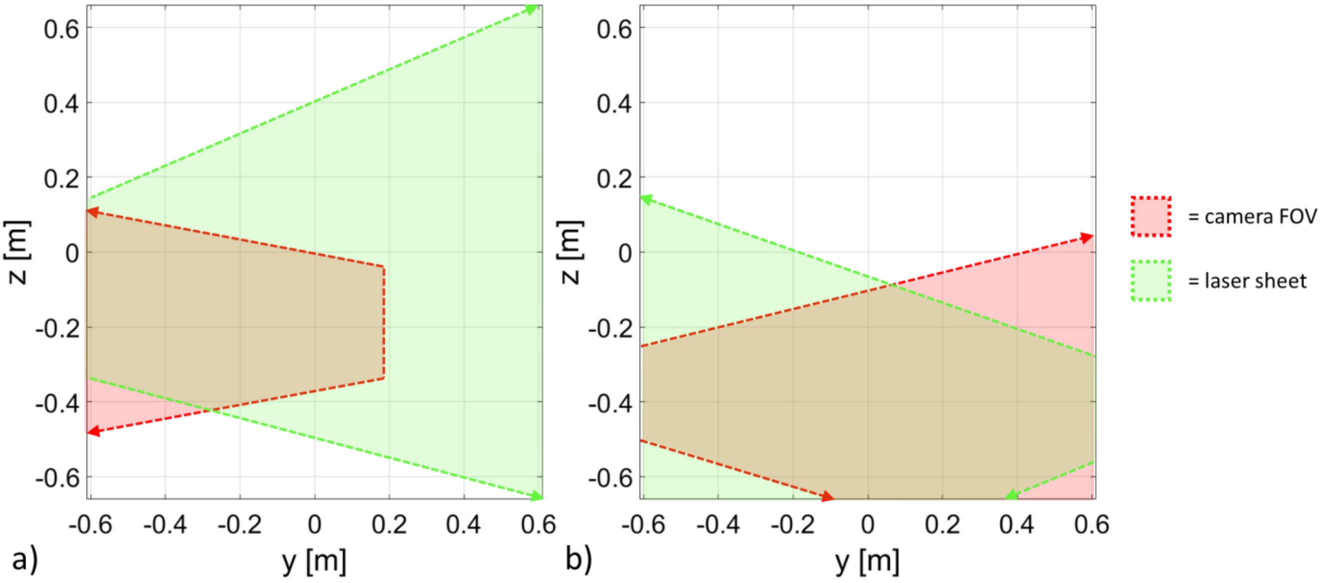

**Fig. 5** Relative positions of camera fields of view and laser sheets within the UPWT cross section. a) Test 1 and b) Test 2.

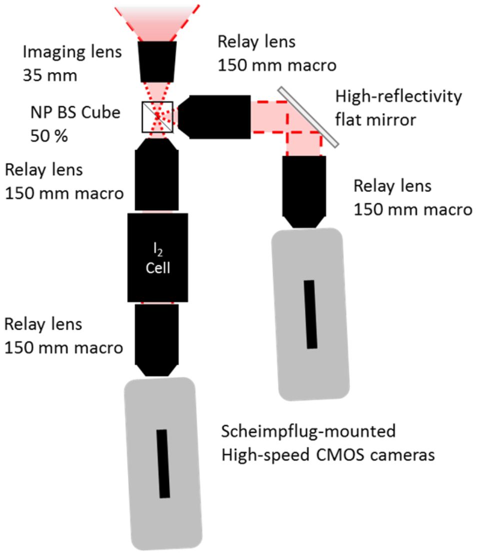

**Fig. 6** Diagram of dual-relay imaging system.

## 3. Results

The two testing campaigns were conducted over a range of Mach and Reynolds number combinations that covered most of the operational envelope of the facility. The data presented in this section will be ordered by the facility Mach number, since the vortices were predicted to emanate from the guide rail for the facility nozzle block, the position of which controls the Mach number. Before presenting the results at large, Fig. 7a shows a few sample fields of data taken at Mach 2.5, Reynolds number of $3.3\times10^6$/m from Test 1. Shown in the main figure is a well-defined counter-rotating vortex pair found in the region bound by $(y,z)$ = ([-0.07,+0.1],[-0.25,0]) m. Additionally, the sidewall boundary layer is visible as the bright region for $y$ < -0.46 m. These data are illustrative of three important points related to the datasets at large from both tests. First, the PLMS data are indicative of many things. Within the tunnel freestream, the number density of the ice crystals scales roughly with the flow (mass) density. Vortices were identified by the absence of signal; vortex cores were visible as small, focused, often-circular voids in intensity. These voids exist because either the particles cannot perfectly track with the large kinematic gradients in these regions, or because an insufficient quantity of the ice crystals is entrained between formation and the measurement region. Another observation related to the PLMS was that the tunnel boundary layers had much brighter scattering than the embordered freestream area. The exact mechanism of this occurrence is unknown; however, it is hypothesized that the ice crystals undergo a phase change (solid to liquid) within the boundary layers. This change both alters the index of refraction of the observed seed and potentially allows agglomeration, which would increase both the physical size and scattering cross-section of the seed material. The result is that the boundary layers appear with high contrast relative to the freestream areas. Finally, the seeding for the PLMS is not strictly homogeneous. Although the seed material circulated through the wind tunnel circuit countless times during data acquisition (undergoing numerous phase changes each loop through the repetitive compression and expansion of the gas), under certain operating conditions the seed would preferentially concentrate in unpredictable ways. For example, at the conditions shown in Fig. 7, the seed material concentrated into wispy streaks throughout the freestream area. Detection of vortices within such a background was challenging and ultimately required viewing the data dynamically to see the effects of the vortex cores in motion.

The second point the images shown in Fig. 7 reveal about these datasets is that the flow is very dynamic. The vortex cores and other features that are present under varying conditions do not have a static or repeatable presentation. Instead, their physical position within the tunnel changes (often moving into or out of the fields of view), their form changes (e.g., vortices change from having two cores to one dominant core or dozens of smaller cores within the same 10-ms of data), and sometimes nothing of note is visible. The paper will try to capture general behaviors as

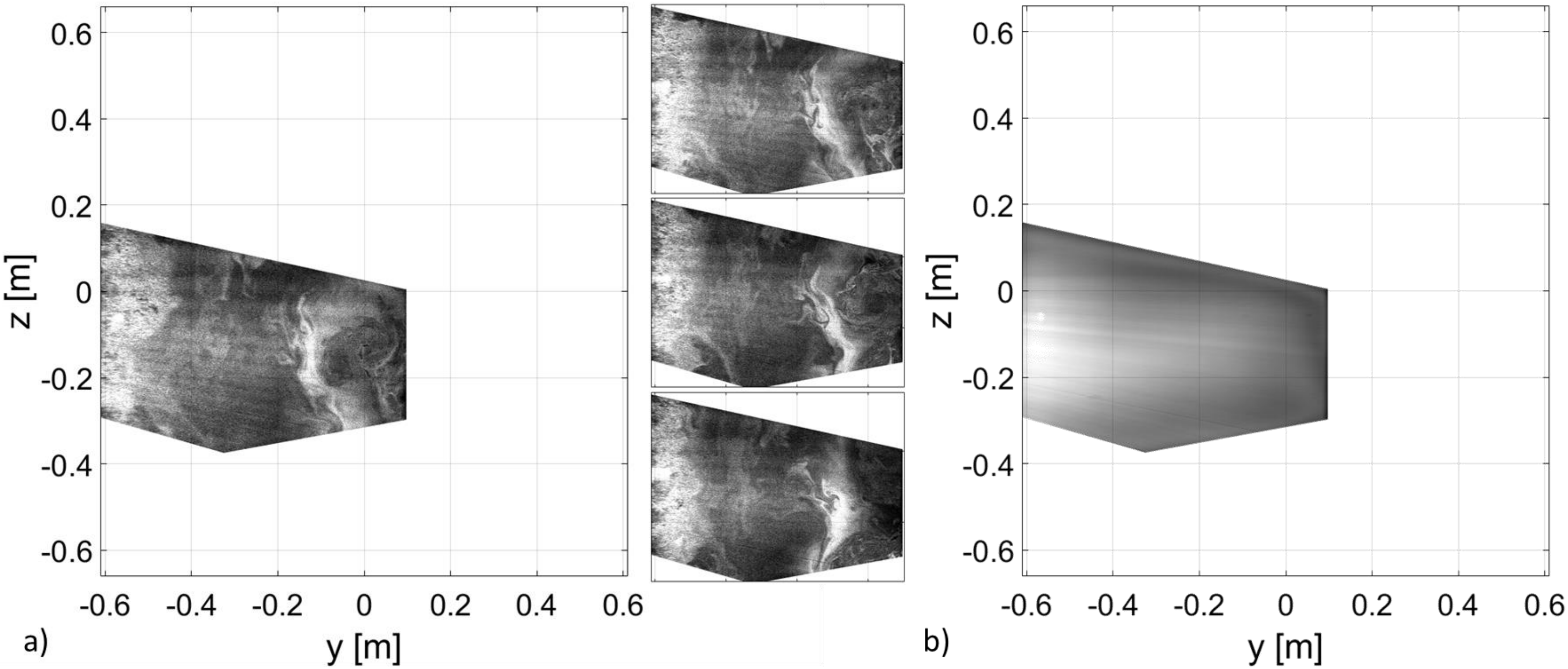

**Fig. 7** Flow visualization data for Mach 2.5, Re 3.3e6/m from Test 1. a) Sample flow visualization from Test 1. Sidebar figures show three additional instantaneous visualizations from within the same laser burst. b) Ensemble averaged image from the same operating conditions. Horizontal striations are from intensity variations in the laser profile.

they vary with tunnel conditions, but this dynamic character and a limited sample size make capturing exacting trends difficult. The third point to make about these data are that perceived flowfield structures do not necessarily imply an underlying flow feature. For example, the appearance of vortices in a particular FOV may indicate the presence of a vortex in the plane, but it may also indicate that a vortex was present upstream (causing the seeding to become inhomogeneous) even if it has already diminished by the measurement plane. Without high-fidelity velocity measurements to assess the local kinematic state of the gas, there is no clear way of making this distinction. Despite this, evidence of the vortices upstream of the measurement location is similarly valuable to assessing the state of the freestream flow. Finally, to demonstrate the value of these instantaneous measurements, a time-averaged version of these data is shown in Fig. 7b at the same tunnel operating conditions, averaged over 50 bursts (though a single-burst average appears similar). It is apparent that, though the vortices and related structures are generally present in the instantaneous images, there is little evidence of their presence in the ensemble-averaged data. The dynamic character of these flow structures necessitates both a high-intensity, short duration laser pulse to capture the instantaneous flow structures and a high-speed measurement strategy to track their motion in time, such as the system that has been implement in these two tests.

The lowest-Mach-number condition tested was at Mach 2.4, Reynolds number of $3.3\times10^6$/m. Data were only acquired during Test 1 at this operating condition, an example of which is shown in Fig. 8. Similar to the example images shown in Fig. 7, a clearly defined counter-rotating vortex structures is visible for $y$ > -0.2 m. Likewise, the sidewall boundary layer can be seen for $y$ < -0.45 m. The observed vortices at this condition were quite mobile and dynamic, frequently shifting vertically throughout the entire FOV. The position shown in Fig. 8 is near the spanwise ($z$-) extremum that was observed in its range of motion. Similar vortex structures were present in approximately half of the acquired images.

At this Mach number, data were also collected at a higher Reynolds number ($9.9\times10^6$/m). Data were acquired during both Test 1 and Test 2 at this operating condition and are shown in Figs. 9 and 10. The Test 1 data showed remarkably little structure at this condition (see Fig. 9a). The predicted vortex cores were visible in only a handful of frames and showed little to no contrast with their surroundings (though faintly visible in Fig. 9a in the regions of ($y$,$z$) = ([-0.05,0.10],[-0.30,-0.18]) m). The data from Test 2 (Fig. 9b) generally suggest that the vortex pair lies primarily in the $+y$ region of the tunnel and rarely (if ever) crosses into the Test 1 FOV. In Fig. 9b, the vortices can be seen as two regions of dark signal amid a bright region (located within ($y$,$z$) = ([0.05,0.25],[-0.30,-0.13]) m). The observed vortices were highly dynamic and chaotic. In addition to extensive lateral and vertical motion covering most of the $+y$ region of the Test 2 FOV, the two vortex cores

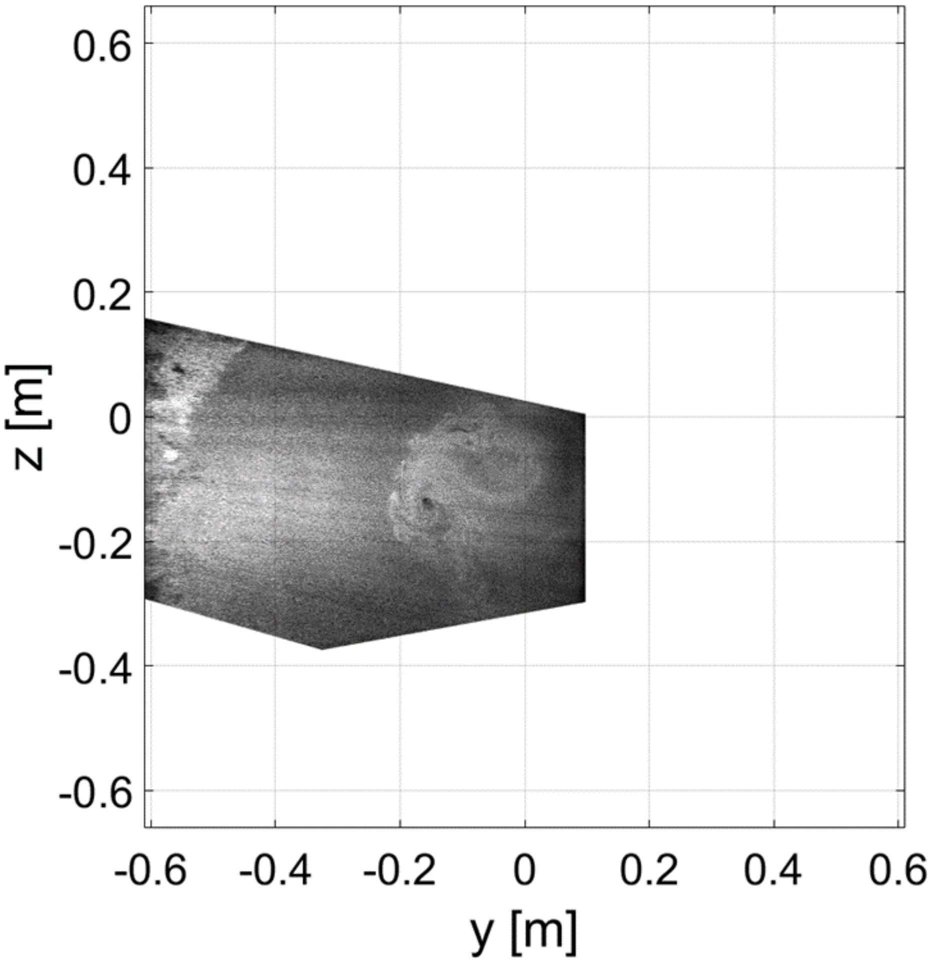

**Fig. 8** Flow visualization data for Mach 2.4 Re 3.3e6/m from Test 1.

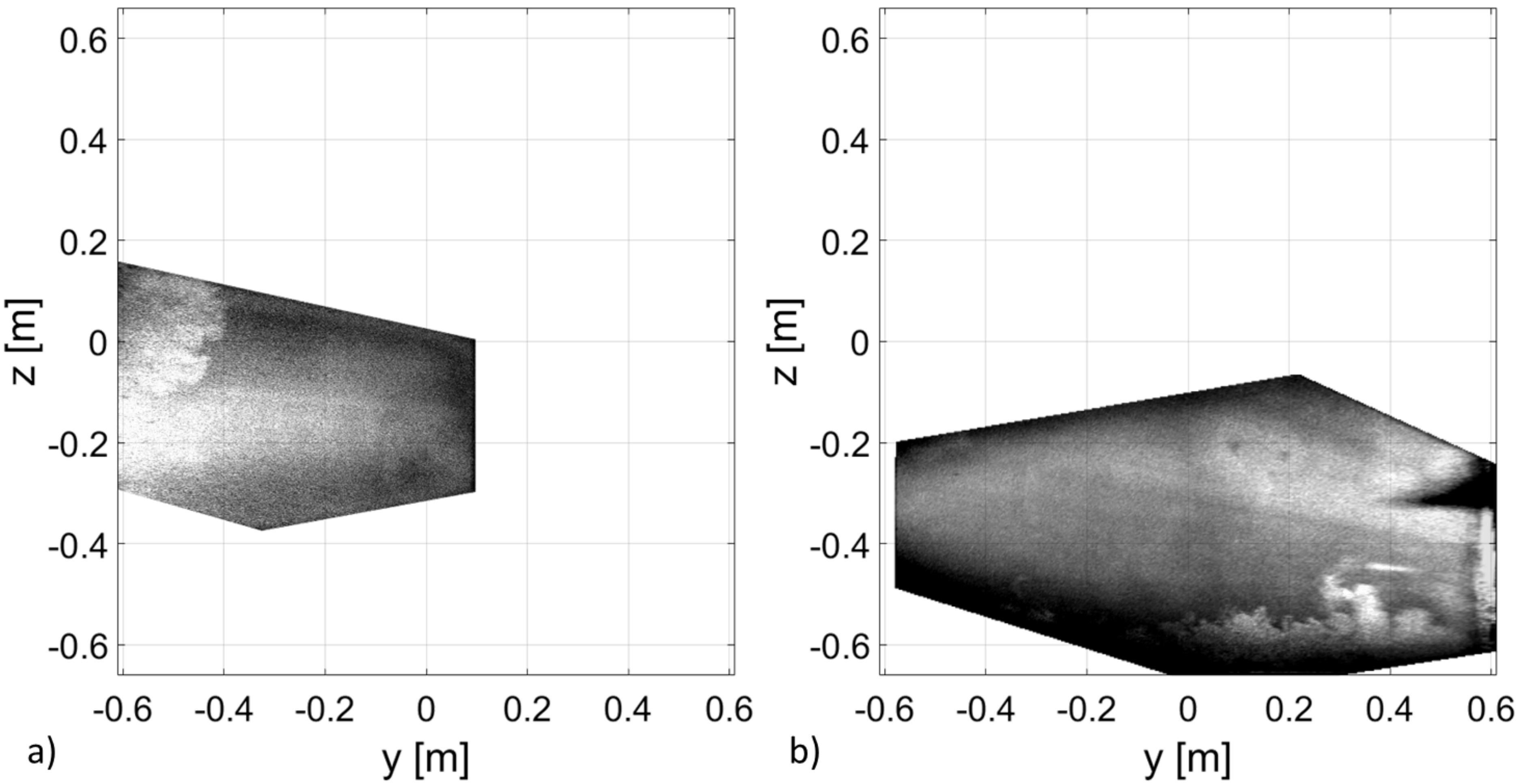

**Fig. 9** Flow visualization data for Mach 2.4, Re 9.9e6/m. a) Test 1 data and b) Test 2 data.

would often revolve around each other, disappear momentarily, or merge. For example, Fig. 10 captures an instance of the vortex pair having descended into the boundary layer and entrained the brighter seed material (located within $(y,z)$ = ([0.05,0.25],[-0.66,-0.3]) m). The vortex cores are inclined at an angle to each other in this instance as well. Finally, no periodic trends to the vortex core motion were apparent. The motion was largely chaotic, and the frequent revolution and merging of the cores make quantifying the motion outside of the frequency of position very difficult or impossible with the limited datasets acquired during these tests. These observations suggest that time-averaged CFD solutions may have difficulty capturing the extent of the vortex phenomenon or may severely underpredict vorticity magnitudes if the feature is present. Time-accurate CFD simulations have replicated this chaotic behavior in part (Childs 2021). The shift in position of the vortices observed between the two different Reynolds number conditions may indicate a medial shift with Reynolds number, but this trend does not appear consistent with data that will be presented further in this section.

Figure 11 shows data captured at Mach 2.5, unit Reynolds numbers of $3.3\times10^6$/m and $9.9\times10^6$/m from Test 1. No data were acquired at this condition during Test 2. Figure 7 also shows sample data at this same condition. Unlike the previous data acquired at Mach 2.4, the vortex pair is clearly visible in the Test 1 FOV at both Reynolds numbers at roughly the same frequency. Because of the position of the vortices in the medial extreme of these FOVs, only the behavior within the -$y$ region could be observed. Similar to the Mach 2.4 case, the observed vortices were highly mobile. When the vortex structure was present in the region, two primary vortex cores were sometimes visible but would often break into multiple smaller cores within a frame or two. Although the total extent of the vortex motion cannot be quantified in this case, the vortices were generally present for locations $y$ > -0.13 m and throughout the entire vertical extent of the FOV for both Reynolds numbers. Although no notable changes were observed in the flow structures, the higher Reynolds number case exhibited more homogeneous seeding. This trend was generally true throughout the tests provided the tunnel dew point was maintained.

Conditions of Mach 2.75 (Re $3.3\times10^6$/m and $9.9\times10^6$/m) and Mach 3 (Re $3.3\times10^6$/m) are shown in Figs. 12 and 13, respectively, from Test 1. These two operating conditions indicate a general transition in the observed behavior of the vortices. At Mach 2.75 (Fig. 12) there isn’t a marked deviation in the behavior of the vortex structure compared to the Mach 2.5 case. The vortex structure is present in about 50 percent of the bursts of data. The size and extent of the motion is comparable as well, and Reynolds number again appears not to affect the flow features significantly). In contrast, the Mach 3 case (Fig. 13) shows a general reduction in both the lateral mobility of the vortex pair and the overall spatial extent of the structure. The lateral motion is

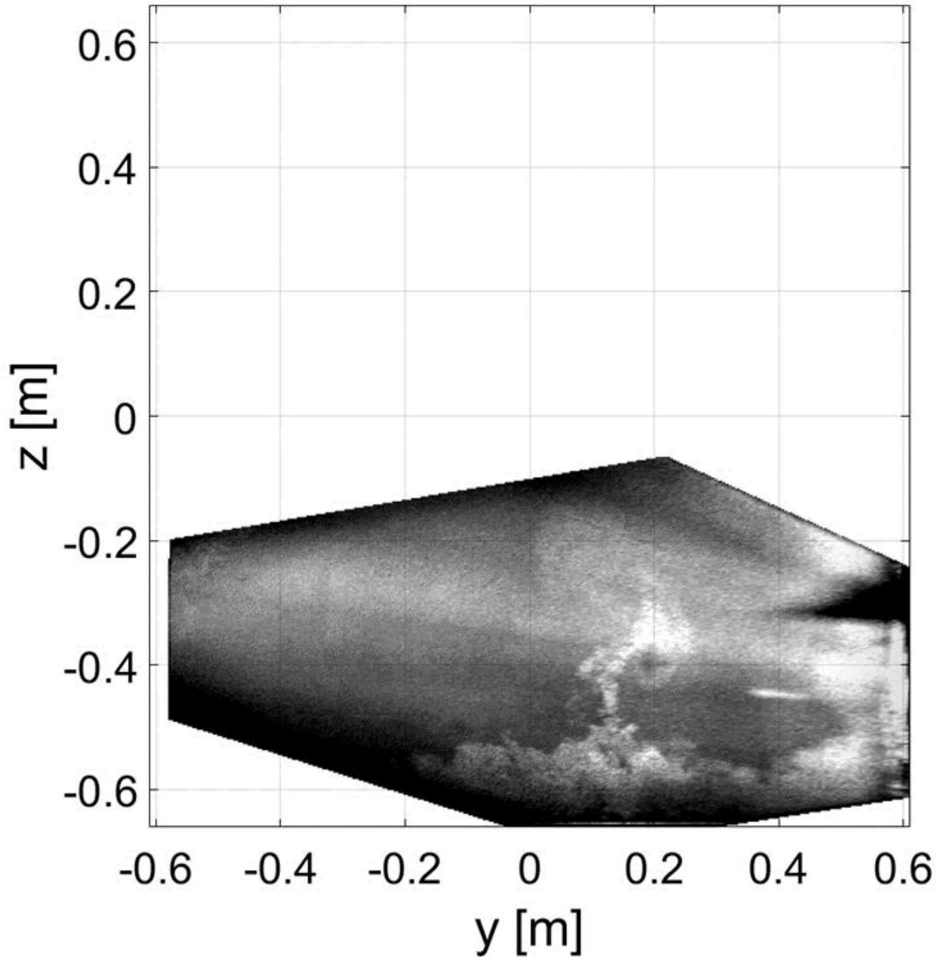

Fig. 10 Flow visualization data for Mach 2.4, Re 9.9e6/ft from Test 2 showing the entrainment of boundary layer fluid by the vortex pair.

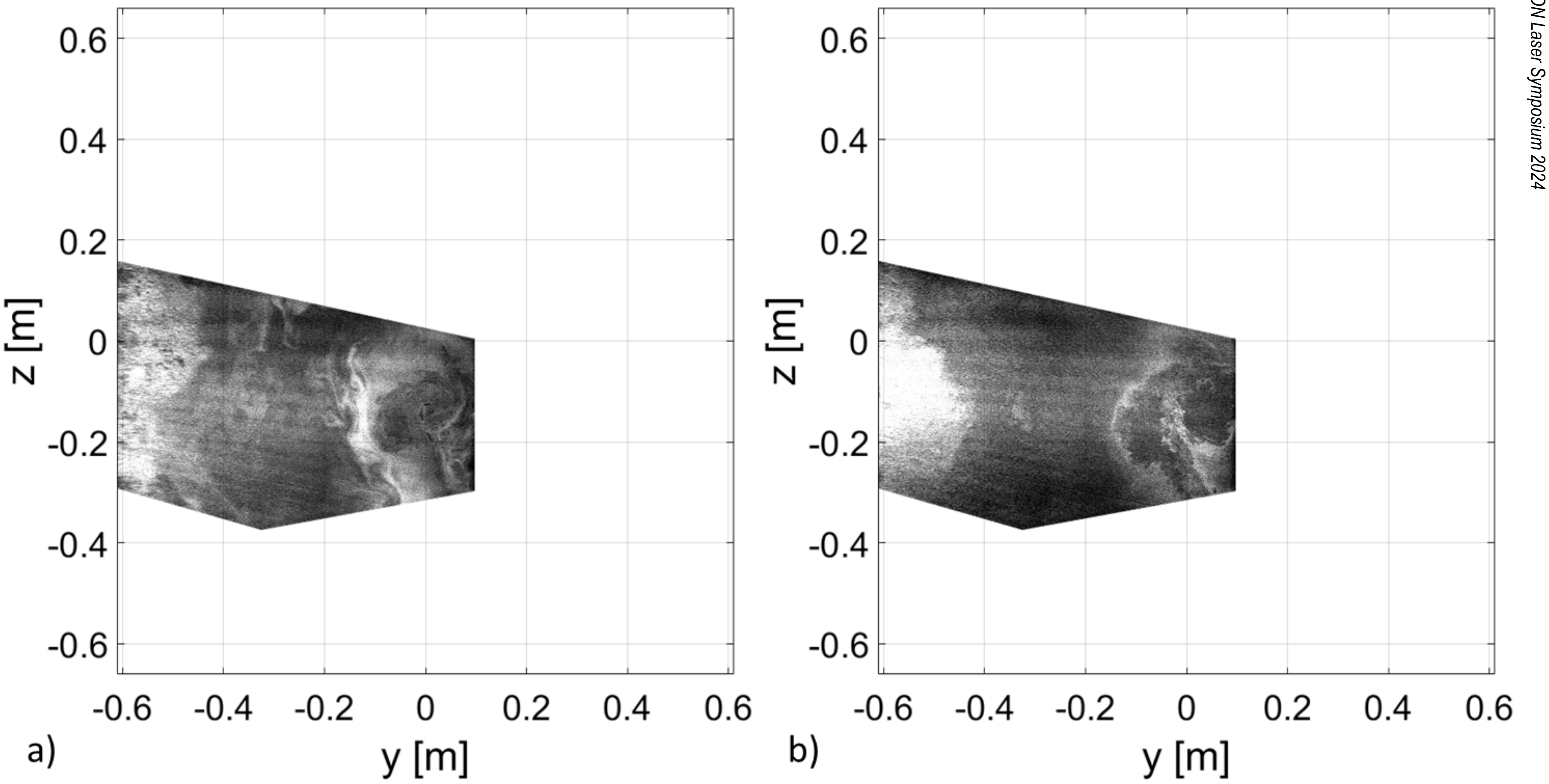

**Fig. 11** Flow visualization data for Mach 2.5 from Test 1. a) Re 3.3e6/m and b) Re 9.9e6/m.

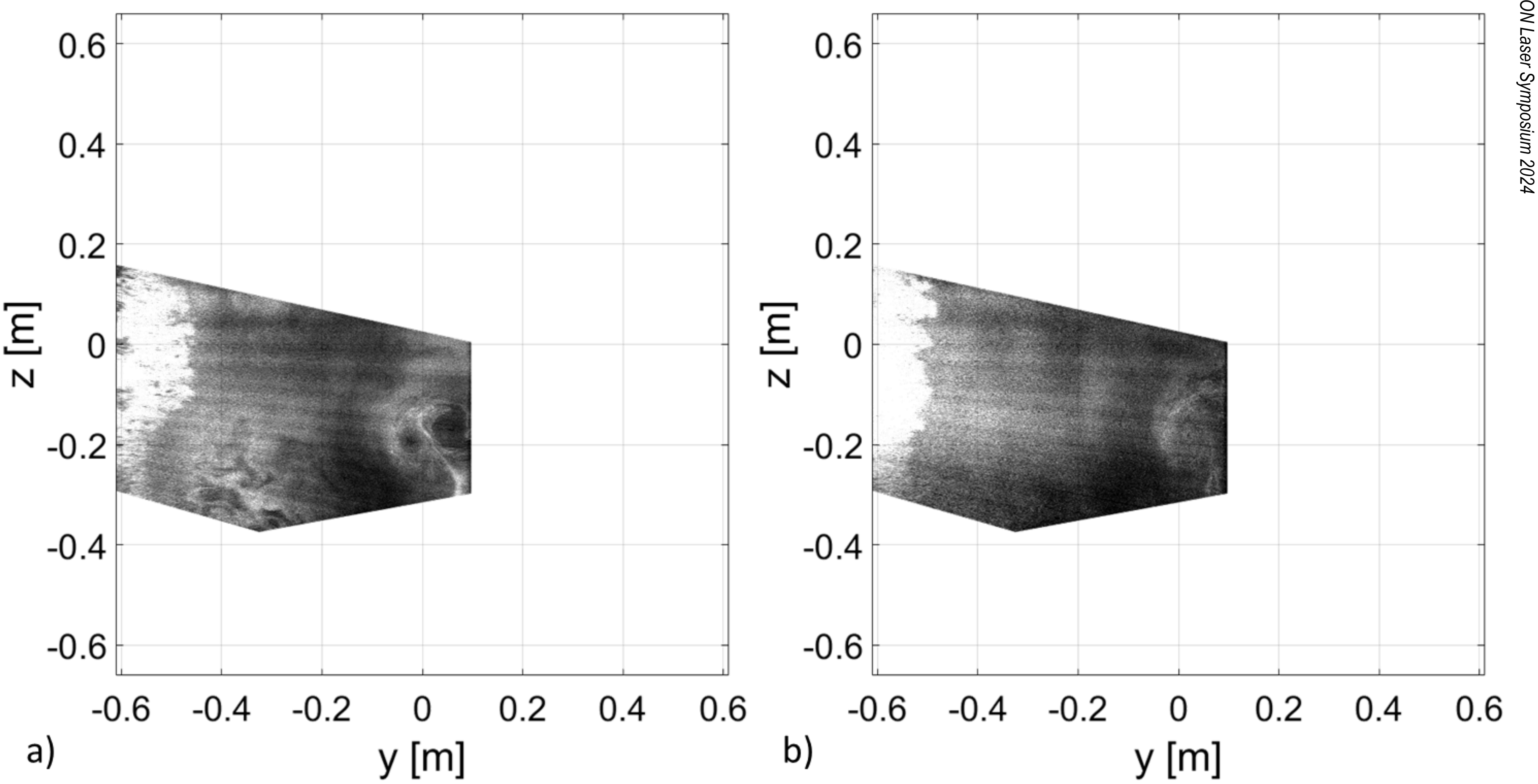

**Fig. 12** Flow visualization data for Mach 2.75 from Test 1. a) Re 3.3e6/m and b) Re 9.9e6/m.

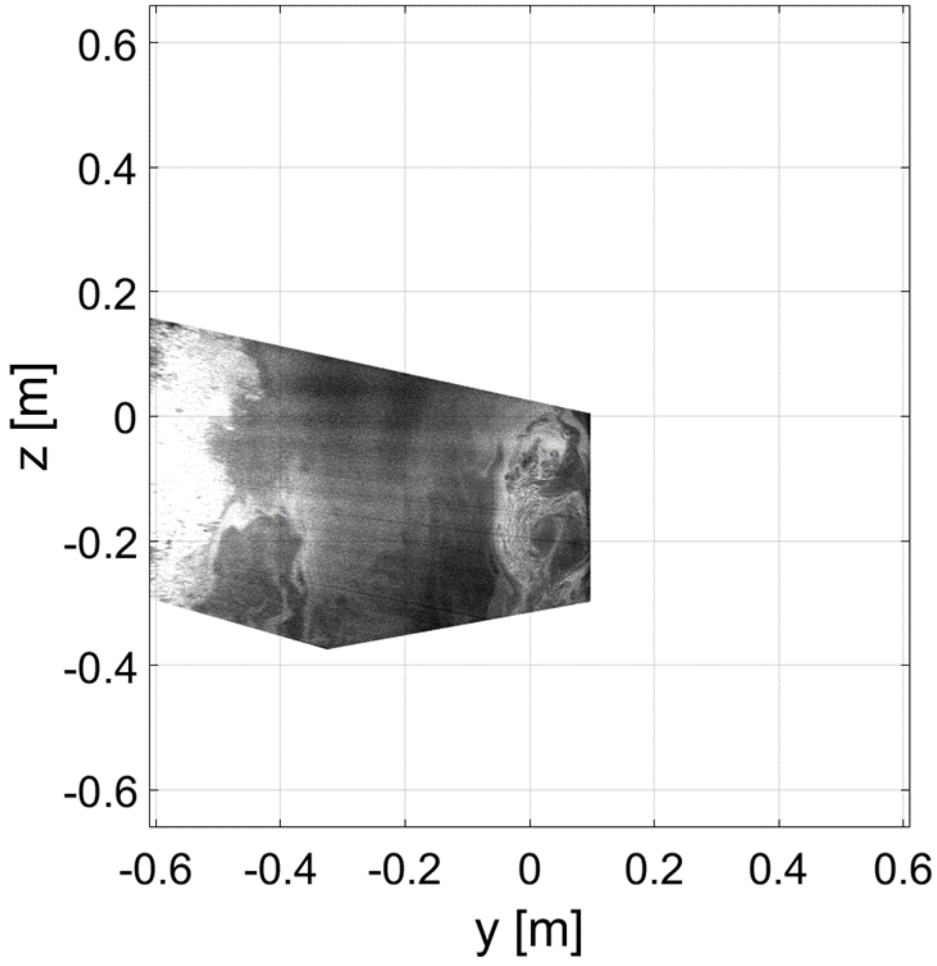

**Fig. 13** Flow visualization data for Mach 3, Re 3.3e6/m from Test 1.

contained between $y$ = -0.05 m and 0.13m, although the vertical extent of the motion is still beyond the bounds of the Test 1 FOV. Furthermore, the vortex structure is nearly always present in the FOV and is present at some point in every burst of data acquired. Compared to the lower Mach number cases, the size of the observed vortex structures is reduced, and the cohesion of the vortex cores is decreased, favoring either a single dominant core or many small vortex cores.

At Mach 3.5, Re 9.9×$10^6$/m, which is shown for Tests 1 and 2 in Fig. 14, the character of the flow has appeared to change entirely. The vortex structures visible in all previously shown cases are no longer present. Instead, the freestream appears largely unperturbed aside from some vertical projection off the floor boundary layer, barely visible in Fig. 14a (region enclosed by ($y$,$z$) = ([0,0.1],[-0.3,-0.18]) m) but more obvious in Fig. 14b because of their position (($y$,$z$) = ([0.05,0.25],[-0.50,-0.38]) m). These structures were observed to oscillated irregularly in the vertical direction, but their spanwise location was consistent burst-to-burst and across time. The abrupt transition from chaotic vortices to relative quiescence in the freestream is likely the result of the position of the nozzle block. At lower Mach numbers, the throat of the nozzle is larger, and thus the nozzle block is positioned closer to the test section. This exposes a larger portion of the guide rail, which is the reason for the formation of these vortices. As the Mach number is increased, the nozzle block is moved closer to the plenum to reduce the throat area, and the T-rail is gradually covered up. The CFD solutions for this condition also indicated a significant weakening of the vortex structures (Childs 2021).

The highest Mach number condition at which data were acquired was at Mach number of 4.6. Data from Test 1 and Test 2 are shown at this condition in Fig. 15. In Fig. 15b, the boundary layer is shown to have generally thickened at this condition. This observation is consistent both with previous probe-based measurements on the tunnel sidewall (Jackson 1981) and simulations (Childs 2021). The previously observed projections from this boundary layer are at roughly the same location but have also increased in vertical extent. This occurrence is likely the result of the greater vertical strain rates in the nozzle block at higher Mach numbers. An interesting new feature has appeared in these data, which are very tall fluid structures, only on the -$y$ side of the tunnel. These are the dominant feature present in Fig. 15a and are present in the same spanwise locations in Fig. 15b with similar high intensity. The spanwise position of these features is consistent burst-to-burst and across time, varying only about 5% of the test section width. These structures, which are being termed ‘sprites’ or ‘fingers’ oscillate vertically quite rapidly, often traversing the vertical extent of the Test 1 FOV in a single frame. At present, it is unknown what these structures are. They have not yet appeared in any of the CFD of the facility and have not been experimentally investigated outside of the present study. As a final note, the semi-oval structure present in the center of the wind tunnel in Fig. 15b is a cross-section of the bow shockwave emanating from a test article above the boundary layer. No data were acquired in the empty freestream during this case, but since the shockwave has not yet interacted with the boundary layer and surrounding structures, it is not believed that the results should differ significantly from an empty tunnel run.

Quantifying the strength of these vortices is not readily achieved with the present measurement systems. The Test 1 studies were set up solely as flow visualizations, since it was unknown whether the vortices would be present in the tunnel. In Test 2, while a velocimetry technique (specifically, the pulse-burst, cross-correlation Doppler global velocimetry (PB-CC-DGV) technique (Burns 2021)) was used, the system was optimized for studying the shock-boundary layer interaction beneath a test article and was principally sensitive to streamwise velocity. Moreover, this technique was burst-averaged, meaning that an average velocity was acquired for each burst of data. Given the extensive and chaotic motion exhibited by the vortices, this technique was unlikely to produce meaningful results. While the more robust CC-DGV velocimetry method could not be utilized, a different type of data analysis was employed to study the velocity, the hybrid pulse-burst/cross-correlation Doppler global velocimetry technique (Burns 2022-2), or hybrid DGV. This method allows for a small number of instantaneous, time-resolved velocity fields to be extracted from PB-CC-DGV datasets. The results of one such frame in which the vortex structure is present is shown in Fig. 16. Figure 16a shows the flow visualization recorded at these conditions, while Fig. 16b shows the corresponding streamwise velocity field. Note that this measurement technique has stringent requirements on the data quality, and thus a large portion of the region of interest did not produce viable results (and thus were omitted from this field). However, the region containing the vortex structure was viable and can be seen in the region bound by $(y,z)$ = ([0,0.25],[-0.38,-13]) m. Strong streamwise vortices would be expected to produce an axial velocity deficit in this context. However, no detail from the vortex pair is visible in the DGV velocity map. Deviations from the background velocity appear to be little more than noise. Statistically, this region exhibits a small (2.4%) *increase* in velocity versus the burst-averaged velocity (552 m/s vs 540 m/s) but is within the local (spatial) noise observed in this region (about 25 m/s, or 4.6% of the measured velocity). Previous estimates on the temporal sensitivity of this technique would also indicate the detection limit somewhere between 7 and 10 percent of the measured velocity for the time step and general quality of the data (Burns 2022-2). For this reason, it’s difficult to make a definitive statement about the strength of the vortices, only that any deficit imparted is below the detection level of this measurement system.

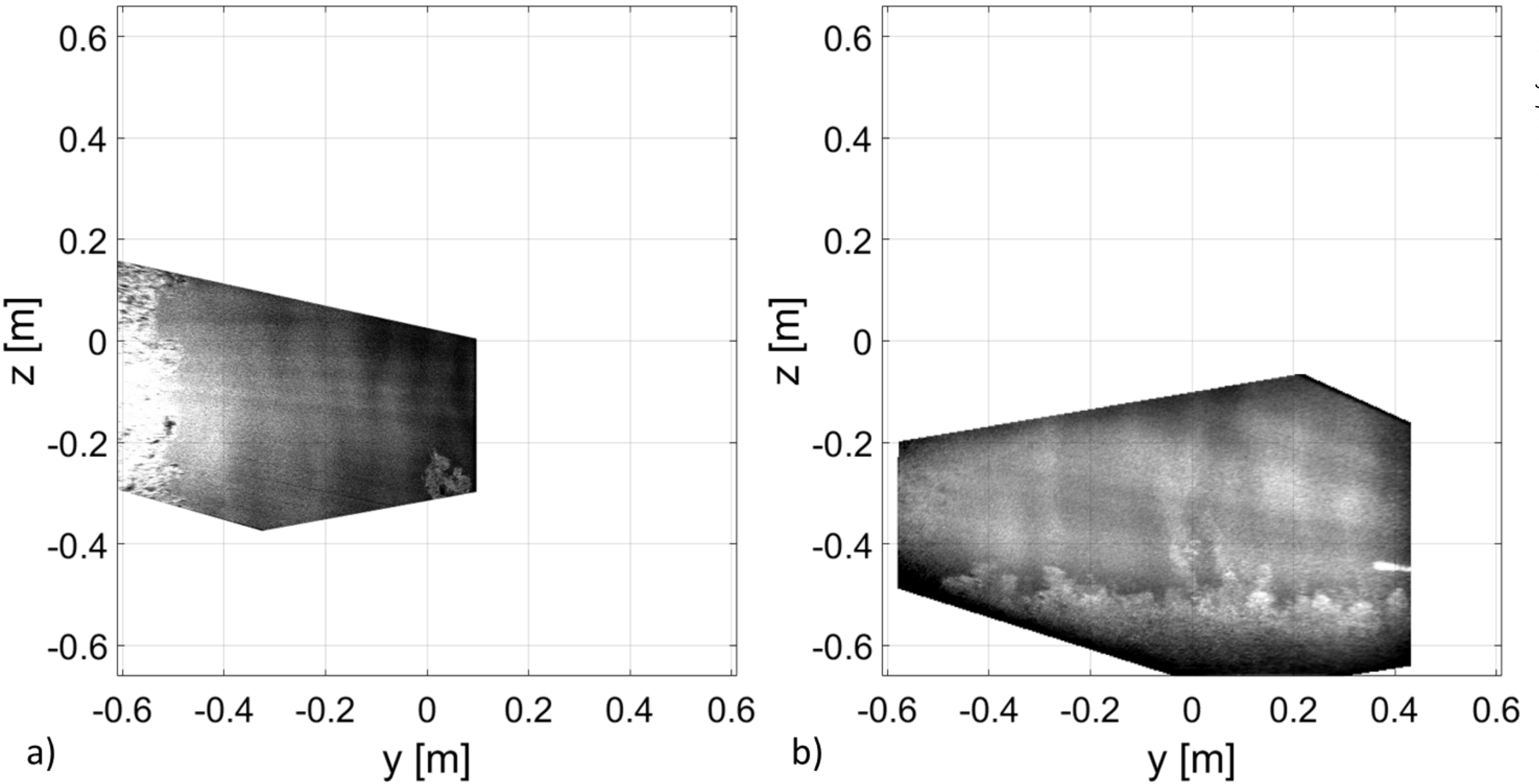

**Fig. 14** Flow visualization data for Mach 3.5, Re 9.9e6/m. a) Test 1 data and b) Test 2 data.

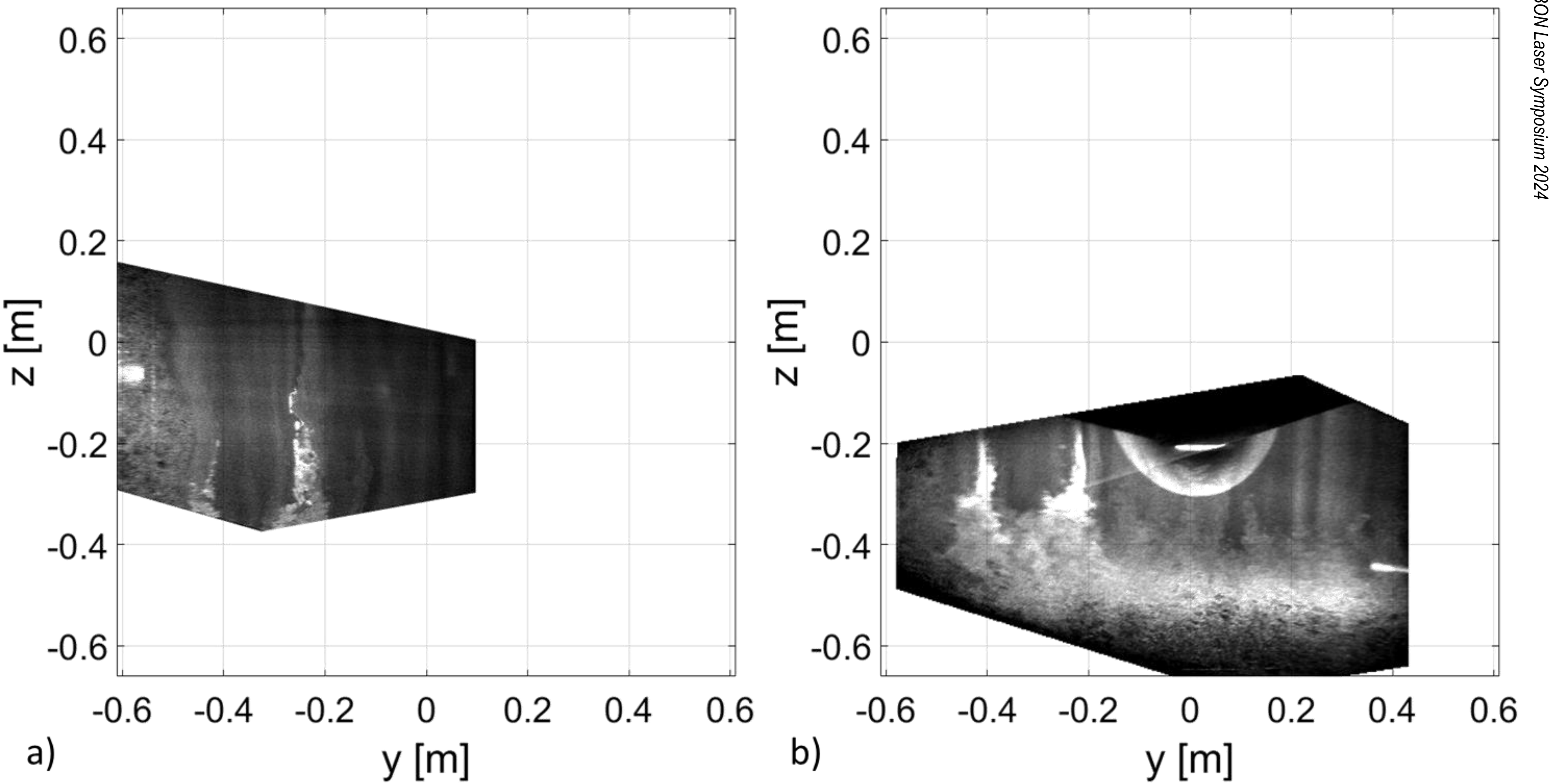

**Fig. 15** Flow visualization data for Mach 4.6 Re 9.9e6/m. a) Test 1 data and b) Test 2 data. In the Test 2 data, the bow shock from a test article is visible in the center of the test section.

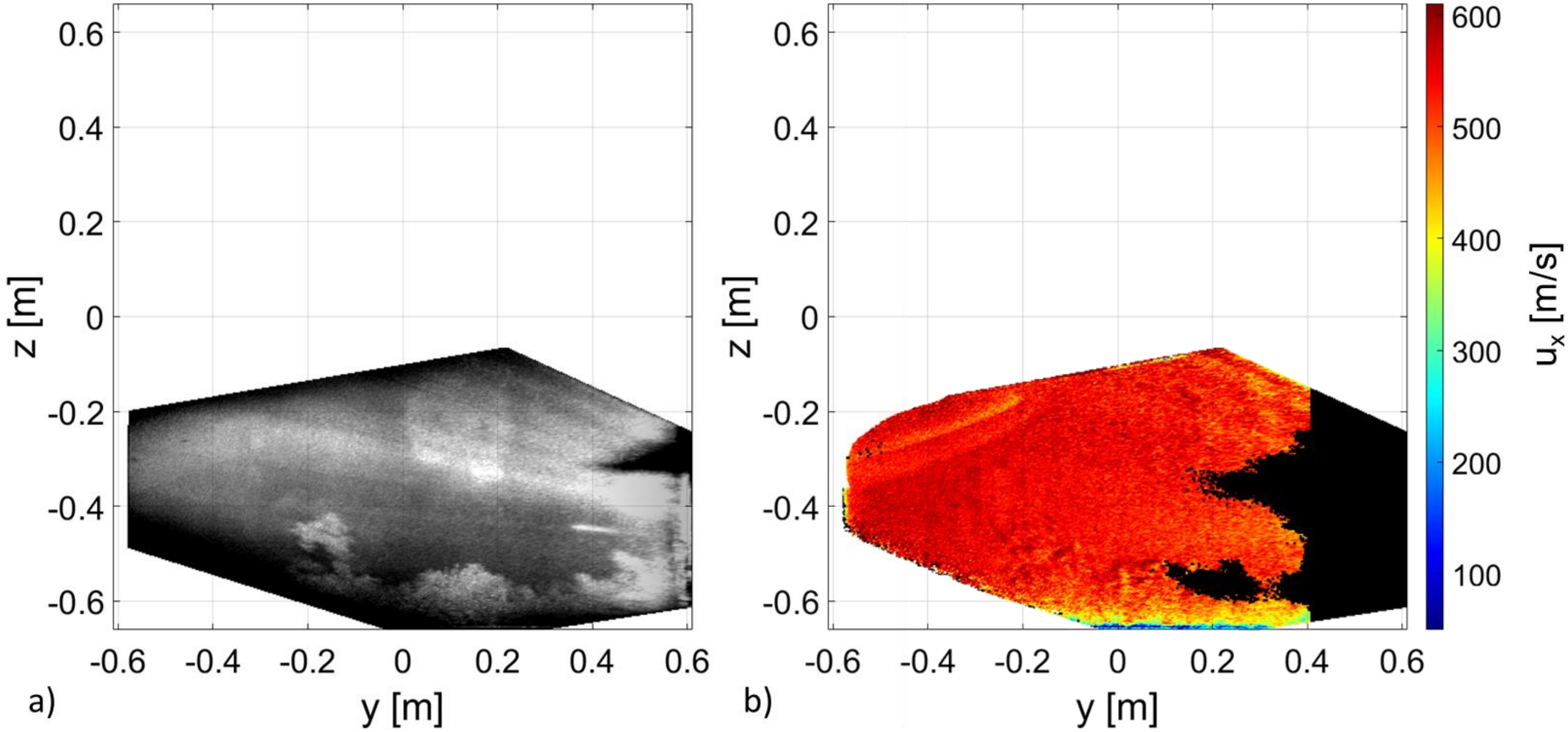

**Fig. 16** Flow visualization and streamwise velocity data for Mach 2.4 Re 9.9e6/m from Test 2 calculated using hybrid PB/CC-DGV. a) Flow visualization and b) Instantaneous velocity contours.

## 4. Discussion

The presence of the freestream vortices was unknown prior to testing. Although vortices appeared in the CFD simulations of the test section, they had not been detected in previous experimental endeavors. In this context, these experiments were successful at both proving that vortices are present in the tunnel freestream under certain conditions and characterizing the conditions and behavior of the vortices. Due to the many unknowns prior to testing, the Test 1 experiments were not optimized to visualize the full range of motion of the vortices. In retrospect, adjusting the FOV to be larger and positioning it closer to the tunnel floor, as was done (arguably to too great an extent) in Test 2, could have improved the fidelity of this dataset. Test 2 was not intended to visualize the freestream but was instead focused on the shock-boundary layer interaction below a test article. It was by coincidence that some freestream data was acquired during these tests, but it proved invaluable at giving context to the Test 1 studies wherever there was overlap. Additionally, the similarity in flow features observed despite the months between these tests bolstered the idea that these were persistent features rather than transient observations.

As for the strength of the vortices, that factor remains largely unknown. The structures visualized through the PLMS measurements are made in a relatively thin plane, and all ‘motion’ that was noted in this paper was initiated far upstream. It is possible that the vortices decay to imperceptible strength before reaching the measurement planes, after having stirred the flow, and caused inhomogeneity in the flow seed that simply appear to be vortices. The hybrid DGV measurements also unfortunately did little to help quantify vortex strength. Due to the large noise and high uncertainty in these measurements, little more than a large bound could be placed to quantify their effect. If it were of interest to the facility, a more targeted set of DGV measurements could possibly be made to quantify vortex behavior (for example, one much more sensitive to the vertical or spanwise velocities), though it is still unclear if the precision of such a system would be sufficient for instantaneous measurements.

Following these experiments, having confirmed the presence of the streamwise vortices, work begin in the UPWT to ameliorate the problem by constructing a fairing that would be positioned over the T-rail in the plenum. This structure is intended to reduce the strength or eliminate the shedding of these vortices to hopefully produce a cleaner freestream. Future measurements are planned to characterize the performance of this fairing in the upcoming years.

## 5. Conclusions

High-speed flow visualizations were performed in NASA Langley’s 4-Foot Supersonic Unitary Plan Wind Tunnel to detect and characterize streamwise vortices present in the tunnel freestream. These tests utilized planar laser Mie scattering to detect inhomogeneity in the tunnel seeded with ice crystals, indicative of vortices and other flow structures. Vortices were found to be present for Mach numbers of 3 or less, with the size and mobility increasing with lower Mach numbers. The effect of Reynolds number on the position and mobility of the vortices was indeterminate; the Mach 2.4

case demonstrated a distinct positional shift at higher a Reynolds number, while the other cases showed no obvious sensitivity to this parameter. At Mach 3.5 and above, the freestream was found to be largely quiescent aside from some sprite-like projections from the floor boundary layer at higher Mach numbers. Hybrid DGV measurements were unable to detect any velocity deficit consistent with the vortex structures, although the particular configuration of the measurement system may have lacked the sensitivity to detect smaller velocity deviations. The detection of these vortex structures has led to facility improvements, with fairing currently begin constructed to limit the strength of these vortices.

## Acknowledgments

The authors would like to thank the tunnel staff at the NASA Langley 4-Foot Supersonic Unitary Plan Wind Tunnel for their help and cooperation in completing these tests. Additional thanks are given to Jim Ross for his continuing support of these research efforts. Funding for this work was through the NASA Aerosciences Evaluation and Test Capabilities (AETC) Portfolio and the NASA Transformational Tools and Technologies (TTT) program, Innovative Measurements discipline.

## References

Birch, TJ, Allen, JM, and Wilcox, FJ (2000). Force, Surface Pressure and Flowfield Measurements on Slender Missiles at Supersonic Speeds. *18th AIAA Applied Aerodynamics Conference*. Denver, CO.

Burns, RA, Fahringer, TW, and Danehy, PM (2021). Velocity measurements across and oblique shock using pulse-burst cross-correlation DGV. *AIAA Scitech 2021 Forum*. Virtual Event.

Burns, RA, Fahringer, TW, and Danehy, PM. (2022). Planar Investigation of a CobraMRV Reentry Flowfield Using Pulse-Burst, Cross-Correlation DGV. *AIAA SciTech 2022 Forum*. Dallas, TX.

Burns, RA, Fahringer, TW, and Danehy, PM. (2022). Hybrid pulse-burst / cross-correlation DGV for high-speed flow measurements at 100 kHz. *20th International Symposium on the Application of Laser and Imaging Techniques to Fluid Mechanics*. Lisbon, Portugal.

Cary, AW, Chawner, J, Duque, EP, Gropp, W, Kleb, WL, Kolonay, RM, Nielsen, E, and Smith, B. (2021). CFD Vision 2030 Road Map: Progress and Perspectives. *AIAA Aviation 2021 Forum*. Virtual Event.

Childs, RE, Stremel, PM, Hawke, VM, Garcia, JA, Alter, SJ, Hunter, C, Kleb, WL, Parikh, P, Patel, M, Rhode, MN, and Salari, K. (2021). Flow Characterization of the NASA Langley Unitary Plan Wind Tunnel, Test Section 2: Computational Results. *AIAA Aviation 2021 Forum*. Virtual Event.

Chou, A, Leidy, AN, and Rhode, MN. (2021). Measurements of Freestream Fluctuations in the Langley Research Center Unitary Plan Wind Tunnel. *AIAA SciTech 2021 Forum*. Virtual Event.

Danehy, PM, Wisser, BM, Fahringer, TW, Winski, CS, Falman, BE, Shea, S, Boyda, M, and Lowe, KT. (2019). Laser Light Sheet Flow Visualization of the Space Launch System Booster Separation Test. *AIAA Aviation Forum 2019*. Dallas, TX.

Denison, MF, Garcia, J, Nikaido, B, Murman, S, Ross, JC, Childs, R, Stremel, P, Kleb, B, Alter, SJ, West, TK, and Robinson, P. (2021). Evaluation of CFD Predictions of CobraMRV Control Surface Effectiveness at the NASA Langley Unitary Plan Wind Tunnel. *AIAA Aviation 2021 Forum*. Virtual Event.

Jackson, CM, Corlett, WA, and Monta, WJ. (1981). Description and Calibration of the Langley Unitary Plan Wind Tunnel. *NASA TP-1905*.

Meyers, JF (1995). Development of Doppler Global Velocimetry as a Flow Diagnostics Tool. *Measurement Science and Technology*. 6(6). 769-783.

Morris, OA, Corlett, WA, Wassum, DL, Babb, CD. (1985). Vapor-Screen Technique for Flow Visualization in the Langley Unitary Plan Wind Tunnel. *NASA TM-86384*.

Ross, JC, Rhode, MN, Falman, BE, Edquist, KT, Schoenenberger, M, Brauckmann GJ, Kleb, B, West, TK, Alter, SJ, and Witte, DW. (2021). Evaluation of CFD as a Surrogate for Mach 2.4 to 4.6 Wind-Tunnel Testing – Project Overview. *AIAA Aviation 2021 Forum*. Virtual Event.

Ross, JC, Denison, MF, Childs, RC, Garcia, JA, Stremel, PM, Hawke, VM, Spooner, HR, Reed, MA, Kleb ,BL, Watkins, AN, Danehy, PM, Burns, TW, Borg, SE, and Robinson, PE. (2021). Evaluation of CFD for Simulation of High-Supersonic Control-Surface Effectiveness. *AIAA Aviation 2021 Forum.* Virtual Event.

Slotnick, JS, Khodadoust, A, Alonso, J, Darmofal, D, Gropp, W, Lurie, E, and Mavriplis, D. (2014). CFD Vision 2030 Study: A Path to Revolutionary Computational Aerosciences. *NASA/CR-20140218178*.